*Journal of Medical Engineering & Technology*, 2012; 36(3): 156–162
Copyright © 2012 Informa UK, Ltd.
ISSN 0309-1902 print/ISSN 1464-522X online
DOI: 10.3109/03091902.2011.645943

informa
healthcare

INNOVATION

# Inductively coupled microfluidic pressure meter for *in vivo* monitoring of cerebrospinal fluid shunt function

S.-H. Song[1], G. T. Gillies[1], M. R. Begley[1,†], M. Utz[1,*], and W. C. Broaddus[2]

[1]*Department of Mechanical and Aerospace Engineering, University of Virginia, Charlottesville VA 22904, USA and*
[2]*Department of Neurosurgery, Virginia Commonwealth University, Richmond, VA 23298, USA*

**A microfluidic pressure sensor with inductively coupled, wireless readout capability has been developed for integration into cerebrospinal fluid shunt valve implants. The sensor consists of a deformable PDMS film that is bonded over a microfluidic reservoir, forming a fluidic capacitor. Deflection of the capacitor membrane is detected remotely through a shift in the resonance frequency of a micro-fabricated LC circuit. Sensors were fabricated by a combination of conventional MEMS technologies and rapid soft lithography. A direct pattern transfer technique was used to pattern the deformable PDMS film with a metal coating for the capacitive readout. The mechanical response of the fluidic capacitor was characterized by measuring the deflection of the PDMS film using an extrinsic Fabry-Perot interferometer (EFPI), and wireless sensing was demonstrated by the shift in resonance frequency of the sensor via an inductively coupled antenna. The sensor transduces pressure into a change in resonant frequency with sensitivity > 3.4 ppm Pa$^{-1}$ and responsivity 4.6 kHz Pa$^{-1}$, over a dynamic range of 0 ~ 3 kPa.**

**Keywords:** CSF shunt, Microfluidic pressure meter, Inductively coupled antenna, Fluidic capacitor, Implantable flowmeter

Copyright © 2012 Informa UK Limited
Not for Sale or Commercial Distribution

## 1. Introduction

The goal of the present work was to develop a microfluidic pressure sensor of sufficient sensitivity to monitor the function of cerebrospinal fluid (CSF) shunt valve implants non-invasively, without the need for leads to cross the skin. Shunt valve implants are commonly used in the long-term management of hydrocephalus. Their main mode of failure consists in gradual obstruction of the flow through protein build-up. With current technology, this is difficult to diagnose without surgically accessing the implant.

The brain and the spinal cord are surrounded by a cushioning layer of cerebrospinal fluid, which is primarily produced and circulated within the four interconnecting cavities of the brain known as ventricles, as well as the spinal cord. These structures produce CSF at a rate of approximately 500 ml per day (approx. 340 µl min$^{-1}$). Hydrocephalus is a neurological disorder associated with an abnormally high intracranial pressure of more than 2.4 kPa, which results from an imbalance between CSF production and re-absorption of CSF into the vascular space.

CSF shunts have revolutionized the treatment for hydrocephalus since their invention almost 60 years ago [1]. While these relatively simple devices have been effective in managing hydrocephalus, they suffer from a high rate of complications due to shunt blockage and infection. Blockages mostly occur within the first year after implantation. Unfortunately, the first sign of shunt failure is the recurrence of clinical symptoms of hydrocephalus, such as headaches and seizures, which can have many other causes as well. Currently, definitive diagnosis of shunt blockage requires a surgical procedure, at considerable risk and discomfort for the patient, as well as cost. The ability to monitor the operation of shunts *in vivo* non-invasively would ameliorate this need.

A conventional shunt consists of a valve separating two catheters going to a ventricle of the brain for CSF access and to the abdominal cavity for drainage, respectively [2]. While in some systems the valve opening pressure can be selected prior to implantation, it is in general not easily adjustable post-operatively, and the CSF pressure cannot be monitored after the implantation.

Passive telemetric pressure sensors based on pressure-modulated resonance of an LC circuit are widely used [3–6]. Recently, as micro-electromechanical systems (MEMS) technology has progressed, miniaturized telemetric pressure sensors have been developed for biomedical applications [5, 7],

*Corresponding author. E-mail: mu3q@virginia.edu

†Current address: Department of Mechanical Engineering, University of California, Santa Barbara, CA 93106, USA

such as monitoring of the intracranial pressure [7], abdominal aortic aneurysm pressure [8], measurements of the intraocular pressure [9], and transcranial pressure [10]. Both the sensing approach through a resonant LC circuit and the enabling micro-fabrication technologies for such MEMS devices are well established [11]. However, most micro-machined capacitive pressure sensors have used a silicon diaphragm. The high modulus of silicon requires large aspect ratios of the membrane, which must be exceedingly thin (less than 1 μm) to ensure adequate pressure sensitivity. This greatly complicates fabrication, and poses concerns of robustness of the diaphragm [12, 13].

In this contribution, MEMS techniques and soft lithography are combined to fabricate a pressure sensor based on a highly compliant elastomer membrane. Such membranes exhibit large, easily detected deflections at small pressures [14], and are commonly used to build fluidic capacitors in microfluidic environments [15].

Our elastomer pressure sensors are fabricated by combined MEMS and direct pattern transfer in a simple and cost-effective manner. In the remainder of this paper, the fabrication process is described in detail. The performance of the sensor membranes is documented for the clinically relevant pressure range from 0.3 to 2.8 kPa, and flow metering in the range of 0–2400 μl $\text{min}^{-1}$ is demonstrated in an on-bench test. Finally, preliminary data are presented that demonstrate wireless pressure sensing which will allow for non-invasive measurements of pressure and flow in a next generation prototype device.

## 2. Materials and methods

### 2.1. Design

The design of the microfluidic flow meter is shown in Figure 1. The fluid is transported in a channel etched into a glass substrate, capped with a layer of poly(dimethyl siloxane) (PDMS). Pressure sensors are located above circular reservoirs with diameters from 2 to 4 mm. Each flow meter consists of a microfabricated inductor coil combined with a plate capacitor, as shown in the figure. One plate of the capacitor is patterned directly onto the PDMS membrane, while the other is integrated with the top support structure, which also carries the inductor. The capacitor gap size varies with the pressure-induced deflection of the membrane, leading to a pressure dependence of the resonance frequency.

Three different sizes of capacitors are embedded with each size of a planar coil inductor. Elliptical shape of capacitors and square shape of inductor are described using the following notation, *C2I3.5*, *C3I4.5*, *C4I5.5*, where *C* is the long axis span of capacitor, 2 mm, 3 mm, 4 mm, and *I* is the side length of inductor, 3.5 mm, 4.5 mm, 5.5 mm, respectively. The separation distance between the top and bottom of capacitor is 50 μm. Dimensions of the microfluidic channels are shown in Figure 1.

The top half of the capacitor is fixed to an upper housing fabricated from glass, which supports a gold layer as the planar coil inductor to create an LC resonant circuit that communicates with the external reader. The motion of the deformable layer can be quantified by shifts in the resonant properties of the LC circuit in relation to internal pressure and then ultimately to flow rate through the channel. The LC resonant circuit characteristics of the sensor can be estimated based on the geometry of the inductor and capacitor by using the equations given by Terman [16]. The capacitance is given by the integrated parallel metal plates with a gap separation at the centre of the sensor. The gap size $d$ between the capacitor plates is given by $d = g - \delta$, where $g$ is the gap size at zero pressure, and $\delta = P/k$ is the deflection of the membrane center in response to the pressure $P$. The membrane stiffness is given by [14, 15]:

$$k = \frac{2\overline{E}t^3(3a^4 + 2a^2b^2 + 3b^4)}{3a^4b^4} \quad (1)$$

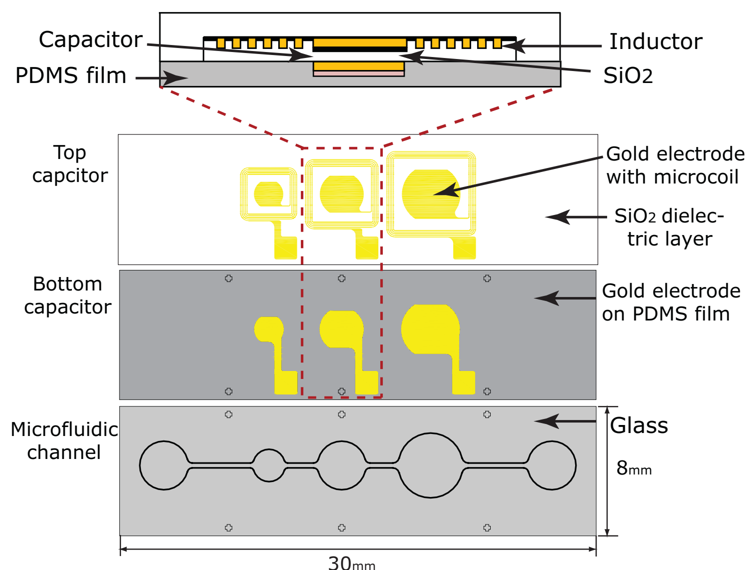


Figure 1. The design of the microfluidic flow meter.

Copyright © 2012 Informa UK Ltd.

where $\bar{E}$ is the plane-strain modulus, $t$ the thickness, and $a$ and $b$ represent the half axes of the elliptically-shaped membrane, respectively. Even though the deflected membrane adopts a non-planar shape, we estimate the capacitance using the plate capacitor equation $C_s = \varepsilon A_0/d$, where $A_0 = \pi ab$ is the surface area of the capacitor and $\varepsilon$ represents the dielectric constant.

The conceptual schematic for the measurement of the passive wireless sensing is shown in Figure 2. The wireless implant device is represented by an RLC circuit, where $R_s$, $L_s$, $C_s$ are resistance, inductance and capacitance of the sensor, coupled to the antenna circuit with inductance $L_a$, tuning capacitance $C_a$, and matching capacitance $C_c$.

The sensor can register pressure variations by means of electrical characteristic changes, which are determined using conveniently formed RLC circuits for frequency-based measurement. The wireless detection of the resonance frequency of the sensor is based on the changes in impedance due to the variations of capacitance of sensor ($VC_s$). The impedance of the secondary reflected to the primary by the inductive coupling and a peak in the secondary impedance corresponds to resonance of the sensor. The sensor as the primary impedance and its coupling to the antenna as the secondary are modelled with a LC frequency-resonance network circuit.

The input impedance of the antenna is expressed with a lumped RLC circuit of the sensor. Transformer network theory using phasor notation ($s = j\omega$) yields equation (2):

$$V_1 = L_a \frac{dI_1}{dt} + M_{12}\frac{dI_2}{dt} \qquad V_1(s) = sL_a I_1 + sM_{12} I_2$$

$$V_2 = M_{12}\frac{dI_1}{dt} + L_s\frac{dI_2}{dt} \qquad V_2(s) = sM_{12} I_1 + sL_s I_2 \tag{2}$$

$$-V_2 - R_s i_2 = \frac{1}{C_s}\int I_2 dt \qquad -V_2(s) = R_s I_2 + \frac{1}{sC_s} I_2$$

where $L_a$ is the antenna inductance, $L_s$ is the sensor inductance, $M_{12}$ is the mutual inductance, $C_s$ is the sensor capacitance, $R_s$ is the sensor resistance, and $V_{1,2}$, $I_{1,2}$ are the voltages and currents, respectively. Solving for $I_2$ yields the input impedance of the equivalent circuit as:

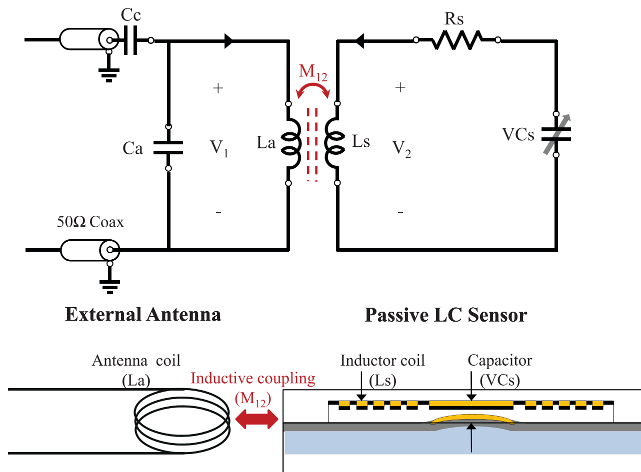


Figure 2. The passive wireless sensing concept.

$$Z_1 = \frac{V_1}{I_1} = j\omega L_a + \frac{\omega^2 M_{12}^2}{R_s + j(\omega L_s - 1/\omega C_s)} \tag{3}$$

From equation (3), $Z_1(s)$ as a transfer function of the equivalent circuit becomes:

$$Z_1(s) = sL_a + \frac{-s^3 M_{12}^2 C_s}{1 + s^2 L_s C_s + sR_s C_s} \tag{4}$$

The sensor was placed in the plane of the antenna loop and the impedance $Z_1(j\omega)$ of the antenna was measured as a function of frequency.

## 2.2. Fabrication

The sensors were fabricated by a combination of conventional MEMS technology and rapid soft lithography [17], as illustrated in Figure 3. Pattern designs were drawn using AutoCAD 2008 and iron oxide/soda lime masks were prepared with resolution/critical dimension tolerance of 4.0 ± 0.5 µm. The top half of the capacitor contained surrounding gold wires as the planar coil inductor. The dimension of planar micro-coil is 50 µm/10 µm (width/thickness) and five turns. As shown in Figure 3 (left), a layer of AZ1500 (Clariant, Charlotte, NC, USA) photoresist 530 nm thick was deposited on borosilicate glass substrate (Telic, Torrance, CA, USA), patterned using UV-lithography, and the photoresist and Cr

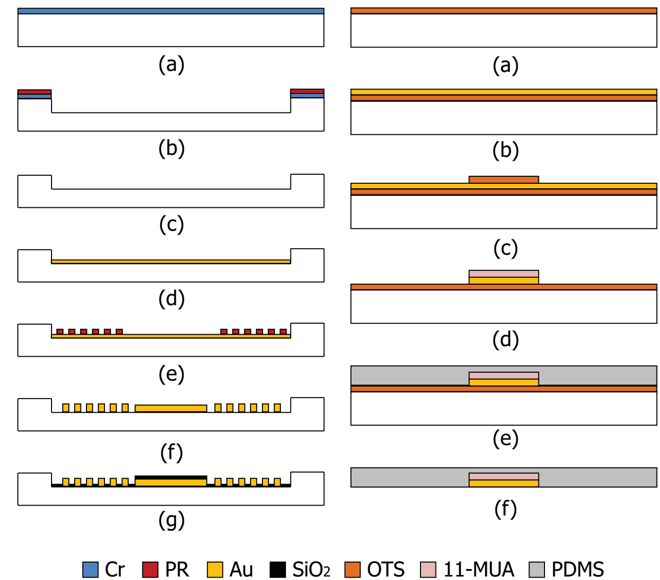


Figure 3. Fabrication processes. (Left side of figure) Top half of the capacitor with the planar coil inductor: (a) Cr deposition (50 nm) on glass wafer; (b) photoresist (AZ1512) patterning and glass wet etching (60 µm); (c) remove photoresist and Cr; (d) Au seed layer deposition (Cr/Au = 50 nm/150 nm); (e) photoresist (AZ4620) patterning and electroplating (10 µm); (f) opening Au electrode, development and photoresist removal, etching of seed layer (Cr/Au); (g) $SiO_2$ deposition (0.1 µm) as a dielectric layer. (Right side of the figure) Bottom half of the capacitor: (a) first SAM treatment using octadecyltrichlorosilane (OTS); (b) Au deposition (Cr/Au = 50 nm/150 nm); (c) photoresist (AZ1512) patterning and Cr/Au etching, and remove PR; (d) 2nd SAM treatment using Mercaptoundecanoic acid (11-MUA); (e) PDMS deposition (150 µm at 1000 rpm) and curing; (f) remove substrate.

layers were removed for glass etching. Since borosilicate glass is an amorphous material, it exhibits isotropic behaviour in wet chemical etching. The efficiency of the chemical etching process, mainly determined by the etch rate, is influenced by three factors: etch solution composition, bath temperature, and stirring. The best etching results were obtained by a HF: $HNO_3$ = 100: 15 (*v*/*v*), volume fraction at 25–40°C, and strong stirring, with an etch rate of 6 μm $min^{-1}$. After etching, the top half of the capacitor with the planar coil was patterned on the substrate using UV-lithography. A seed layer consisting of a Cr/Au film (50 nm/150 nm thickness) was deposited using a CMS-18 thin film deposition system (Kurt J. Lesker, Philadelphia, PA, USA). The top electrode was patterned and electroplated to 10 μm of Au. To form electrical insulation between the electrodes, silicon oxide as a dielectric material was deposited using plasma enhanced chemical vapour deposition (Plasma-Therm, Saint Petersburg, FL, USA). The bottom half of the capacitor is shown in Figure 3 (right). Wafer cleaning starts with the typical SPM sequence. The surface of a p-type silicon wafer is modified with SAM (self-assembled molecular monolayer) treatment. A SAM solution combined OTS (Octadecyltrichlorosilane, $CH_3(CH_2)_{17}SiCl_3$, Sigma) with toluene, 95: 5 (*v*/*v*), volume fraction. The wafer was immersed into the solution for 3 h and then rinsed with toluene. After the surface OTS treatment, a Cr/Au film, 50 nm/150 nm thickness, was sputtered on the modified surface and patterned via a photolithographic process. The hydrophobic surface modified by OTS treatment formed the activated releasing layer. The metal patterned wafer was modified with a second SAM treatment. The wafer was immersed in a second SAM solution, 5 mM 11-MUA (Mercaptoundecanoic acid, $HS(CH_2)_{10}CO_2H$, Sigma) in ethanol, for 1 h and then rinsed with ethanol. This process can make metal patterns with a strong bonding to the polymer surface [18]. A pre-polymer base and a curing agent, Sylgard 184 (Dow Corning, Midland, MI, USA), were thoroughly mixed using a volume ratio of 9: 1. Air bubbles were removed from the mixture using a degassing chamber. A clear PDMS layer was spin-coated (at 1000 rpm, 150 μm) on the metal patterned wafer and cured on a hotplate at 100°C for about 1 h. The cured PDMS film with the embedded metal patterns, gold coated on PDMS film, is separated from the wafer by the lift-up method and then bonded to the microfluidic channel using plasma surface treatment. Finally, Figure 4 shows the micro-fabricated gold coated on PDMS film-based pressure sensor.

## 2.3. Experimental set-up

### *2.3.1. Deflection measurement*

Film deflections were measured using an extrinsic Fabry-Perot interferomery (EFPI) spectrometer (Luna Innovations, Blacksburg, VA, USA). A broadband luminescent emitting diode, operating at 830 nm maximum wavelength, was coupled to the deflection sensing optical fibre and aligned orthogonal to the microfluidic chip with gold coated on PDMS film on a vertical moving stage (Z-axis) with angle adjust lever (Edmund Industrial Optics, Barrington, NJ, USA). Reference and sensing reflections returned through the fibre, which was coupled to a miniature spectrometer consisting of a diffraction grating and a CCD array. This decoupled the interference pattern to provide optical path length (OPL) between all of the reflecting surfaces in the light path. The OPL corresponding to the deflection of the gold coated on PDMS film was isolated and fed back into the EFPI spectrometer. Frequency analysis of the signal was performed via FiberPro software.

### *2.3.2. Wireless sensing*

The assembled sensors were tested on-bench to characterize their wireless sensing performance. The sensor was placed on a plastic holder and magnetically coupled to an external antenna. The antenna consisted of a planar, circular coil with an outer diameter of 5 mm wound from magnet wire (Belden 8052, St. Louis, MO, USA). The coil width/space/thickness/turns are 0.5 mm/0.1 mm/0.5 mm/3, respectively, resulting in a self-resonant frequency around 680 MHz. The antenna was connected to both ports of a network analyser (HP8753D, Agilent, Santa Rosa, CA, USA) by a 50 Ω coaxial cable. The wireless sensing configuration is shown in Figure 5. A beaker is filled with deionized (DI) water for operation in liquid. Hydraulic pressure is generated by supplying DI water from the beaker to the inside of a microfluidic channel under the PDMS film and the external antenna is aligned above the sensor on the same manipulation stage for *in situ* wireless sensing. The resonant frequency of the sensor was monitored by

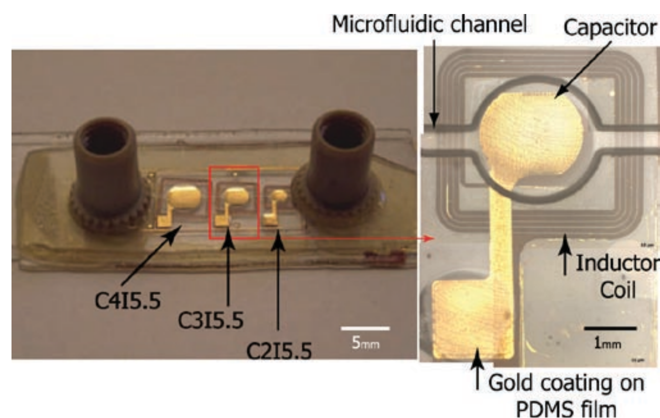


Figure 4. Images of the micro-fabricated devices.

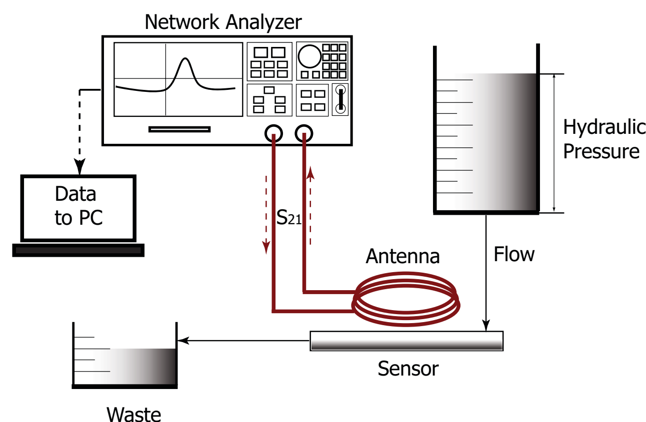


Figure 5. The wireless sensing configuration for the on-bench system.

Copyright © 2012 Informa UK Ltd.

tracking the frequency of the characteristic peak in the transmission loss $S_{21}$ on the network analyser.

In this study, the antenna, Φ = 5 mm, has an inductance of roughly 13 nH and the self resonance frequency is 680 MHz. At resonance, the sensor induces a change in impedance $Z_1$. The initial resonance peak change occurs at 672 MHz, 658 MHz, 654 MHz with *C2I3.5*, *C3I4.5*, and *C4I5.5*, respectively.

## 3. Results and discussion

### 3.1. Mechanical characterization

Fluidic capacitance is related to the deflection of PDMS film in response to fluid pressure. The relationship between the deflection and pressure acting on the film is described by equation (1). Figure 6 shows the deflections of the PDMS films in response to fluid pressure as measured by EPFI, and compares them to the theoretical prediction based on the nominal dimensions of the sensors.

The measured values of E = 670–680 kPa for the modulus of PDMS film are obtained from the best fit of the data in Figure 6. These values can represent the possible range of the calculated response, with the nominal value 750 kPa (a curing agent vs. the polymer mixing ratio = 1: 10) [19], with a 10% variation in modulus of the PDMS film.

### 3.2. Electrical characterization

The shifts of the resonance peaks were measured with a wired interface to the network analyser due to pressure change at room temperature. The resonance frequencies of the sensor LC circuits were measured by placing the sensor capacitor and inductor in series between the ports of a network analyser, and determining the peak value of the transmission loss ($S_{21}$), as a function of the fluid head pressure applied to the device. The resulting resonance frequencies with the wired interface are shown in Figure 7. As expected, the values decrease with increasing pressure, due to the pressure-induced increase in capacitance of the LC circuits. At a given pressure, the resonance frequency of the smallest sensor is the highest, starting at about 420 MHz at zero pressure, compared to 175 MHz for the largest sensor. In the range from 0 to 1 kPa, the resonance frequencies decrease approximately linearly with pressure, with an initial slope of about 200 MHz/kPa in all cases.

The shaded areas shown in Figure 7 represent the allowable range of the calculated peak frequencies using equation (1), for the PDMS modulus obtained from the deflection measurements with a 10% increase variations. It is clearly seen that the measured values match well within the shaded areas with the calculated response at higher pressure.

### 3.3. Wireless readout of pressure

The response of the sensors to pressure changes was observed wirelessly by coupling to an antenna coil as described above. The antenna coil exhibits a self-resonance in the vicinity of 680 MHz. Placing a sensor directly above the antenna coil, as shown in Figure 5, results in a reduction of the self-resonance frequency of the antenna which depends on the resonance frequency of the sensor, and therefore the pressure. Figure 8 shows experimental $S_{21}$ response curves of the antenna coupled to different sensors at various pressures. The shifts are quite small, but can be clearly detected. However, the data should be regarded as preliminary. A much more sensitive way to observe the sensor resonance would be to couple a small antenna loop at the end of a coaxial cable inductively to the sensor coil, and monitor the return loss. Assuming a large enough quality factor of the resonator, a clear negative peak in the return loss would be observable close to the self resonance frequency of the oscillator. In the present case, it was not possible to observe the resonance in this manner because the quality factor of the microfabricated resonators was not sufficient. This is probably due to the conducting paste that was used to make electrical contact between the upper and

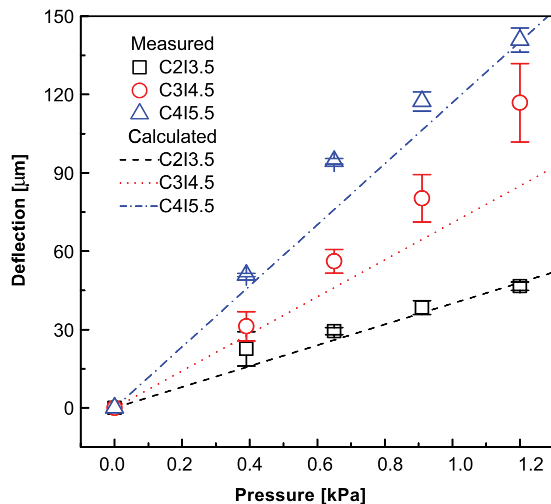


Figure 6. Deflection versus pressure relationship of the PDMS film as the bottom half of the capacitor. Each measured datum represents the average of three independent experiments ($n = 3$) with standard errors of the mean ($p < 0.05$).

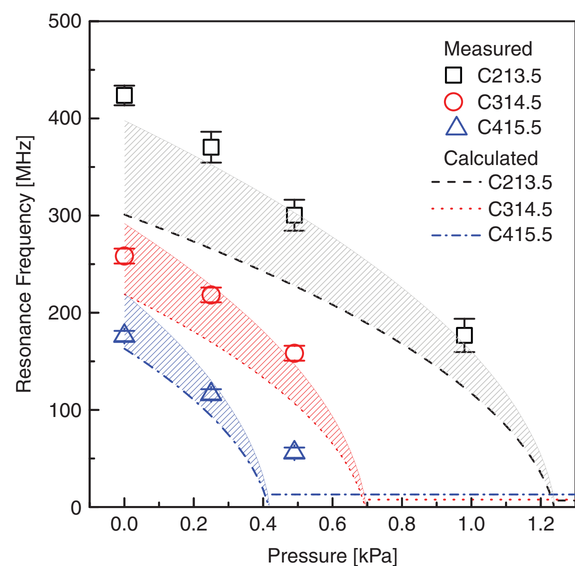


Figure 7. Resonance frequency versus pressure relationship of the capacitor in LC circuit response measured with the wired interface. Each measured datum represents the average of three independent experiments ($n = 3$) with standard errors of the mean ($p < 0.05$).

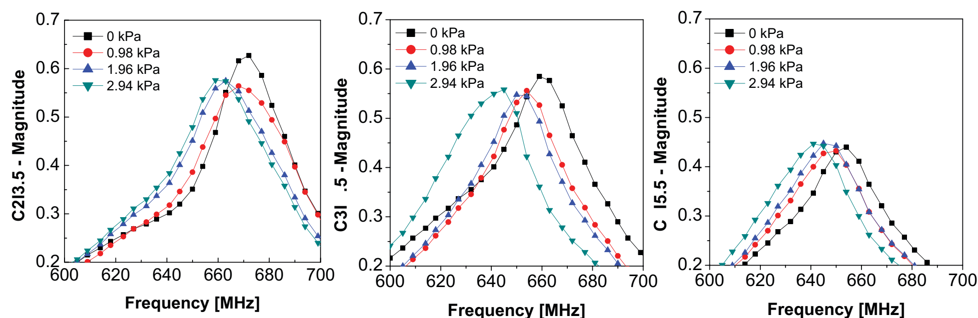


Figure 8. Overlay plots of frequency response curves with wireless interface. The antenna complied to the sensors with three different sizes (*C2I*3.5, *C3I*4.5, *C4I*5.5) of the fluidic capacitors.

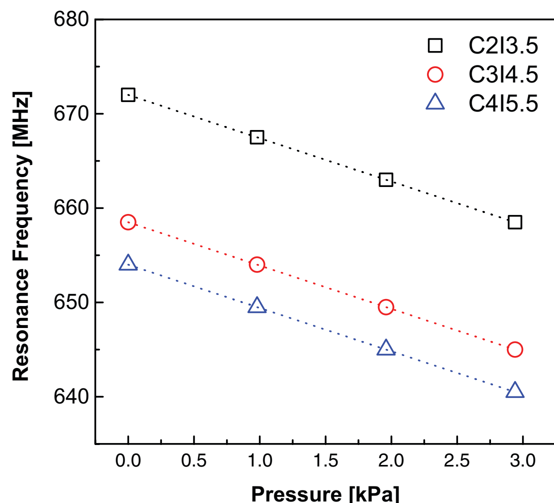


Figure 9. Resonance frequency versus pressure response for wireless sensor.

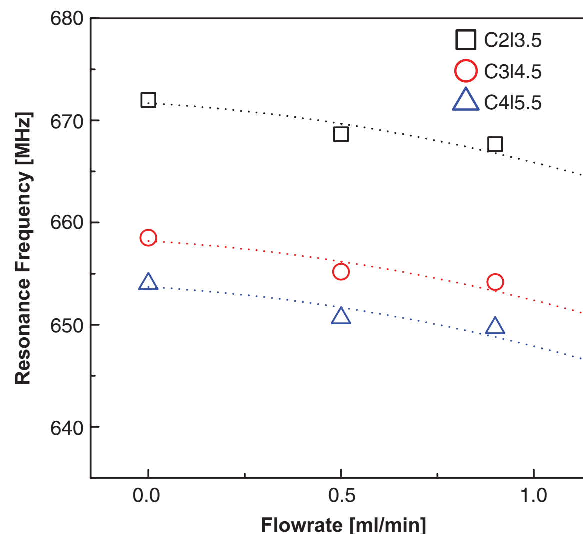


Figure 10. Resonant frequency versus flow rate for wireless sensor.

lower layers of the system. Future designs will use a different interconnect method, which should result in substantially larger *Q*.

The measured antenna self-resonance frequencies from each sensor are shown in Figure 9 as a function of pressure. The pressure dependence is well represented by a straight line with a slope of 4.6 MHz $kPa^{-1}$ for all three sensors. Accuracy of data acquisition is 4 MHz $pt^{-1}$ (frequency span: 800 MHz, 201 pts) during the 430 ms sweep time.

This responsivity of the sensor is higher by a factor of two than previously reported data for several types of telemetry pressure sensors, such as ceramic diaphragms [5], silicon diaphragms [7], and polyurethane membranes [20]. The sensitivities (relative frequency change per kPa pressure change) are better than 3400 ppm $kPa^{-1}$.

### 3.4. Relation of pressure, equivalent flow rate, and resonance frequency

Since the flow resistance of the fluidic network in the sensor is constant, the resonance frequency can also be calibrated against flow rate. Differential pressure sensing is used as the flow sensing principle. Our pressure sensor described here can be utilized for sensing the flow rate. Measuring the deflection of the PDMS film using EFPI with hydraulic static pressure flow and dynamic volumetric flow, we can obtain the relation between pressure and flow rate at the same deflection positions. Figure 10 shows dynamic responses of the resonant frequency and flow rate for the wireless sensors. The resonant frequencies of the sensors decrease linearly in the small volumetric flow range (<1.0 ml $min^{-1}$), but decrease rapidly in the larger flow ranges. Hence, the pressure is proportional to the flow rate at small ranges; the results are similar for the resonant frequency and pressure response trends in the low pressure range.

## 4. Conclusions

In this paper, we have developed a microfluidic flow meter consisting of telemetric pressure sensors that respond to the pressure induced deformation of a PDMS film. The sensors are fabricated by combined conventional MEMS technologies and rapid soft lithography. The bottom half of the capacitor is micro-fabricated on a gold coated PDMS film by a direct pattern transfer technique. The developed sensors exhibit a responsivity of 4.6 kHz $Pa^{-1}$, and sensitivity > 3400 ppm $kPa^{-1}$ over the pressure range of 0 ~ 3 kPa. Remote sensing has been demonstrated in principle through pressure-induced changes in the impedance of an antenna loop coupled inductively to the sensors. In the current design, the sensors exhibit poor electromagnetic quality factors, most likely due to the use of conductive paste

Copyright © 2012 Informa UK Ltd.

to close the tank circuit loop. It is anticipated that substantially better performance could be achieved with higher *Q*.

Future work will be focused on improving the sensing performance by improving the *Q* and introducing more advanced external antennae. In addition, the effect of real CSF on the wireless pressure sensors for practical applications will be studied, and the design will be integrated with existing CSF shunt valve implants in preparation for eventual clinical evaluation.

## Acknowledgements

This work was funded in part by the Biomedical Innovation Fund which is sponsored by the University of Virginia's Department of Biomedical Engineering and the Ivy Foundation, as well as by the National Institute of Health (NIBIB) through grant number 5R01EB011591 - 02.

***Declaration of interest***: Authors Gillies, Begley, Utz and Broaddus may receive royalties through licensing agreements for the intellectual properties associated with this technology, as negotiated by their institutions.

## References

[1] Drake, J., Kestle, J., and Tuli, S., 2000, CSF shunts 50 years on–past, present and future. *Child's Nervous System*, **16**, 800–804.

[2] Drake, J. and Sainte-Rose, C., 1995, The Shunt Book. (Cambridge, Massachusetts: Blackwell Science).

[3] DeHennis, A., and Wise, K., 2005, A wireless microsystem for the remote sensing of pressure, temperature, and relative humidity. *Journal of Microelectromechanical Systems*, **14**, 12–22.

[4] Shin, K., Moon, C., Lee, T., Lim, C., and Kim, Y., 2005, Flexible wireless pressure sensor module. *Sensors and Actuators A: Physical*, **123**, 30–35.

[5] Fonseca, M., English, J., Von Arx, M., and Allen, M., 2002, Wireless micromachined ceramic pressure sensor for high-temperature applications. *Journal of Microelectromechanical Systems*, **11**, 337–343.

[6] Kaiser, T., 2006, Passive telemetric readout system. *IEEE Sensors Journal*, **6**, 1340–1345.

[7] Akar, O., Akin, T., and Najafi, K., 2001, A wireless batch sealed absolute capacitive pressure sensor. *Sensors and Actuators A: Physical*, **95**, 29–38.

[8] Fonseca, M., Allen, M., Kroh, J., and White, J., 2006, Flexible wireless passive pressure sensors for biomedical applications. *Solid-State Sensors, Actuators, and Microsystems Workshop*., Hilton Head Island, South Carolina, June 4–6, 2006. (San Diego, California: Transducer Research Foundation), pp. 37–42.

[9] Chen, P., Rodger, D., Saati, S., Humayun, M., and Tai, Y., 2008, Microfabricated implantable parylene-based wireless passive intraocular pressure sensors. *Journal of Microelectromechanical Systems*, **17**, 1342–1351.

[10] Shah, M., Phillips, R., and Normann, R., 2002, A study of printed spiral coils for neuroprosthetic transcranial telemetry applications. *IEEE Transactions on Biomedical Engineering*, **45**, 867–876.

[11] Chung, S., Kim, J., Wang, K., Han, D., and Chang, J., 2003, Development of MEMS-based cerebrospinal fluid shunt system. *Biomedical Microdevices*, **5**, 311–321.

[12] Chau, H., and Wise, K., 2002, An ultraminiature solid-state pressure sensor for a cardiovascular catheter. *IEEE Transactions on Electron Devices*, **35**, 2355–2362.

[13] Ko, W., and Wang, Q., 1999, Touch mode capacitive pressure sensors. *Sensors and Actuators A: Physical*, **75**, 242–251.

[14] Begley, M., Utz, M., and Komaragiri, U., 2005, Chemo-mechanical interactions between adsorbed molecules and thin elastic films. *Journal of the Mechanics and Physics of Solids*, **53**, 2119–2140.

[15] Leslie, D., Easley, C., Seker, E., Karlinsey, J., Utz, M., Begley, M., and Landers, J., 2009, Frequency specific flow control in microfluidic circuits with passive elastomeric features. *Nature Physics*, **5**, 231–235.

[16] Terman, F., 1943, Radio Engineers' Handbook. (New York: McGraw-Hill).

[17] Duffy, D., McDonald, J., Schueller, O., and Whitesides, G., 1998, Rapid prototyping of microfluidic systems in poly (dimethylsiloxane). *Analytical Chemistry*, **70**, 4974–4984.

[18] Kim, J., Takama, N., Kim, B., and Fujita, H., 2009, Optical-softlithographic technology for patterning on curved surfaces. *Journal of Micromechanics and Microengineering*, **19**, 055017.

[19] Armani, D., Liu, C., and Aluru, N., 1999, Re-configurable fluid circuits by PDMS elastomer micromachining. Twelfth IEEE International Conference on Micro Electro Mechanical Systems. *MEMS'99*, Orlando, Florida, January 17–21, 1999. (IEEE: Piscataway, New Jersey), pp. 222–227.

[20] Takahata, K., and Gianchandani, Y., 2008, A micromachined capacitive pressure sensor using a cavity-less structure with bulk-metal/elastomer layers and its wireless telemetry application. *Sensors*, **8**, 2317–2330.

Copyright of Journal of Medical Engineering & Technology is the property of Taylor & Francis Ltd and its content may not be copied or emailed to multiple sites or posted to a listserv without the copyright holder's express written permission. However, users may print, download, or email articles for individual use.